

Demonstration of Strong Near-Field Radiative Heat Transfer between Integrated Nanostructures

Raphael St-Gelais,[†] Biswajeet Guha,[†] Linxiao Zhu,[‡] Shanhui Fan,[‡] and Michal Lipson^{*,†,§}

[†]School of Electrical and Computer Engineering, Cornell University, Ithaca, New York 14853, United States

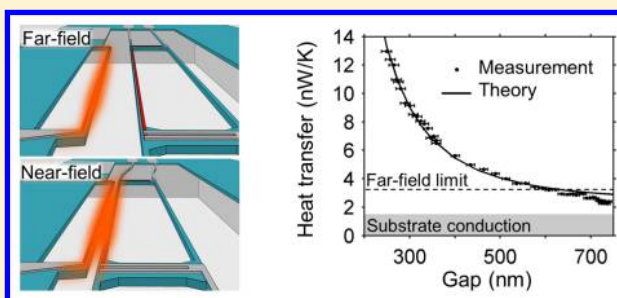
[‡]Ginzton Laboratory, Stanford University, Stanford, California 94305, United States

[§]Kavli Institute at Cornell for Nanoscience, Cornell University, Ithaca, New York 14853, United States

S Supporting Information

ABSTRACT: Near-field heat transfer recently attracted growing interest but was demonstrated experimentally only in macroscopic systems. However, several projected applications would be relevant mostly in integrated nanostructures. Here we demonstrate a platform for near-field heat transfer on-chip and show that it can be the dominant thermal transport mechanism between integrated nanostructures, overcoming background substrate conduction and the far-field limit (by factors 8 and 7, respectively). Our approach could enable the development of active thermal control devices such as thermal rectifiers and transistors.

KEYWORDS: Thermal transport, thermal radiation, near-field radiation, microelectromechanical systems (MEMS), surface phonon-polariton



Recently, there has been a growing interest in controlling radiative heat transfer in the near-field,^{1–11} for applications in thermal microscopy,^{12–14} thermophotovoltaic energy generation,^{15–18} noncontact cooling,^{19,20} and heat flow control.^{21–28} Near-field heat transfer occurs when objects supporting surface phonon-polaritons (e.g., SiO₂ and SiC) or infrared plasmon-polaritons (e.g., doped silicon) are brought to submicron separation, such that their surface modes can evanescently couple. This heat transfer occurs over a narrow frequency range (as opposed to the broadband nature of solid state conduction) and can exceed the blackbody limit by several orders of magnitude.

It has been shown theoretically that near-field heat transfer can enable active functionalities such as thermal rectifiers,^{21–23,25–27} thermal transistors,²⁸ and thermal switches;²⁴ however, these devices would only be relevant to actual systems if shown to occur in integrated geometries, where unfortunately other conduction channels might dominate, rather than in macroscopic object. To date, near-field heat transfer has only been shown using macroscopic objects, i.e., one or two semi-infinite surfaces,^{7,8,10–15,19} or a large probe tip approximated as a sphere.²⁰ Scaling up these macroscopic geometries to an actual thermal circuit composed of several components would be extremely challenging since even a single thermal transistor requires at least two near-field heat transfer junctions. On-chip integration is therefore necessary for the development of several applications. Moreover, miniaturization could eventually yield fundamental performance advantages over macroscopic experiments. For example, nanopatterned objects can significantly relax the distance requirement for efficient near-field heat

transfer between two objects,⁹ while size-induced discretization of thermal modes could allow ultrahigh contrast rectification of heat transfer.²⁷

Here we show strong near-field radiative heat transfer in a novel on-chip geometrical configuration of two parallel suspended nanobeams where the distance between the beams can be tuned electrostatically. Our geometrical configuration is shown in Figure 1a. We use silicon dioxide (SiO₂) for its surface phonon polariton resonances, at 495 and 1160 cm⁻¹, shown to allow near-field heat transfer.^{7,8,11,20} Silicon nitride (Si₃N₄) is used solely for mechanical purposes as its tensile residual stress (~950 MPa) allows for long suspended nanobeams that are thermally isolated from the substrate. We use platinum (Pt) resistors both as resistive heaters and as thermometers to measure the amount of heat transfer.

The gap between the two nanobeams is tuned using a monolithically integrated microelectromechanical (MEMS) actuator (see Figure 2a). Electrostatic actuation is chosen for its negligible power consumption and hence negligible parasitic heat generation. When an actuation voltage is applied, the electric field across the two actuation capacitors induces an attraction force that brings the suspended part of the actuator closer to the fixed heated beam (see Figure 2b). The design of the MEMS, in particular the use of deposited metal electrodes over a nitride mechanical platform, was inspired in part by ref

Received: August 22, 2014

Revised: October 30, 2014

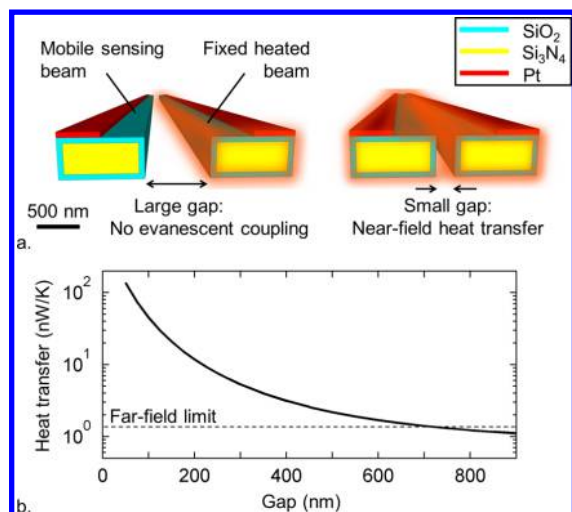


Figure 1. (a) Schematic representation of the experiment. At small gap, evanescent surface polariton resonances at the SiO₂ surfaces couple to enable near-field radiative heat transfer between the nanobeams. Si₃N₄ is used for mechanical purposes, while Pt is used both as a resistive heater and a temperature sensor. (b) Theoretical prediction of the heat transfer between two nanobeams of 200 μm length and 500 nm \times 1.1 μm cross-section. The SiO₂ thickness in this case is 100 nm.

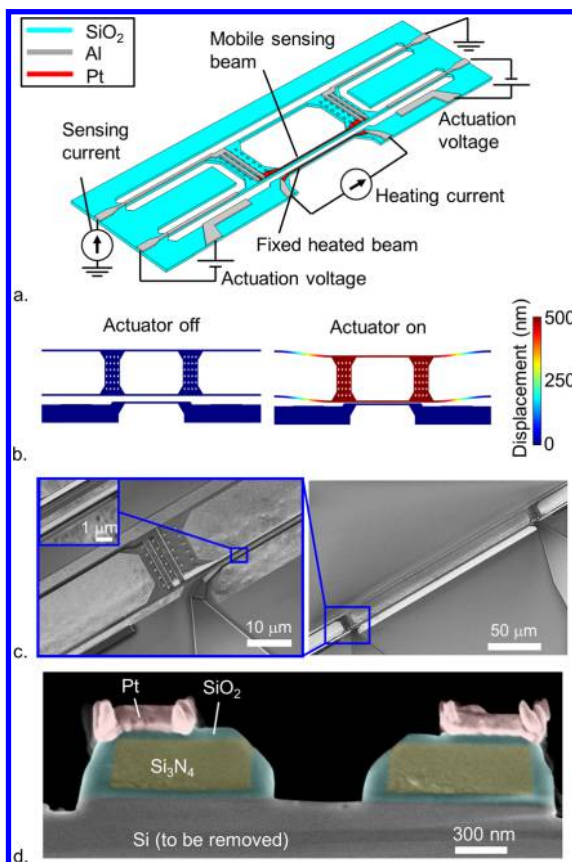


Figure 2. (a) Schematic (not to scale) and electrical circuit of the two-nanobeam system integrated with the MEMS actuator. (b) Schematic (not to scale) of the MEMS displacement. (c) Scanning electron micrographs (SEM) of the device. (d) False color SEM of the nanobeam cross section prior to substrate removal.

29. To tune the gap continuously while avoiding electrostatic pull-in effect, the gap between the electrodes of the actuation capacitors (3 μm) is designed to be more than three times larger than the maximum possible displacement (given by the gap between the nanobeams, designed to be 700 nm). The length of the fixed beam, the mobile sensing beam, and each of the four MEMS suspension springs is 200 μm . Such large dimensions are required to minimize the mechanical stiffness of the suspension springs and hence to allow full range displacement with an actuation voltage below 200 V. These large dimensions are also beneficial to the thermal isolation of the nanobeams (i.e., to the minimization of the background thermal heat conduction between the nanobeams and the substrate).

The simulated heat transfer power between the nanobeams presents a drastic enhancement of heat transfer in the near-field (see Figure 1b). The near-field simulation in Figure 1b is performed using a Fourier modal method based on the fluctuational electrodynamics formalism,^{30,31} considering beams of 200 μm length and 500 nm \times 1.1 μm cross section (including a 100 nm thick SiO₂ coating). The temperature difference between the nanobeams is 130 K (as in our experimental results), with the mobile sensing beam maintained at room temperature. Repeating the near-field simulation while replacing the Si₃N₄ core with SiO₂ shows that the Si₃N₄ core has a negligible effect on the heat transfer compared with a beam that would be made entirely of SiO₂. The insensitivity of heat transfer to the core material results from the surface wave nature of the SiO₂ surface phonon-polariton that dominates heat transfer at small gaps. In the gap range of Figure 1b, the heat transfer power approximately scales as $1/\text{gap}^{1.68}$. At much smaller distances (i.e., distances much smaller than the beam dimensions), we expect the heat transfer to be proportional to $1/\text{gap}^2$, as for parallel plates.¹⁹ The far-field value in Figure 1b is the total far-field emission, integrated over all directions and all frequencies, for a nanobeam maintained at 130 K above room temperature. This value is calculated by the Fourier modal analysis method for a periodic array of nanobeams with a periodicity much larger than the size of nanobeams, such that they do not interact with each other.

The structure is fabricated using conventional nanofabrication processes, which consist of low pressure chemical vapor deposition (LPCVD) of SiO₂ and Si₃N₄, and electron-beam evaporation of platinum resistors and aluminum electrical contacts. The fabrication process begins with the successive deposition of 100 nm of SiO₂, 300 nm of Si₃N₄, and 100 nm of SiO₂ on a virgin silicon wafer. The MEMS and nanobeams are then defined by deep ultraviolet lithography and etched in CHF₃ + O₂ chemistry using an inductively coupled plasma reactive ion etching (ICP-RIE) reactor. Following this etch step, a third layer of SiO₂ is deposited, again by LPCVD, in order to conformally cover the sidewalls of the etched structures. This layer is then anisotropically etched (using the same ICP-RIE chemistry) to clear the bottom of the trenches for subsequent isotropic release, while leaving some SiO₂ on the sidewalls of the nanobeams (see the final nanobeams cross section in Figure 2d). Platinum and aluminum are then successively deposited over the defined structure by electron beam evaporation and lift-off. The aluminum layer is chosen to be much thicker (250 nm) than the platinum layer (60 nm), such that the resistance of the aluminum contacts is negligible compared with the platinum resistors. The higher electrical conductivity of aluminum, relative to platinum, also contributes

to make the resistance of the aluminum contacts negligible. The structure is finally released in XeF_2 gas isotropic etching of silicon. Release holes are included on the larger parts of the MEMS (see Figure 2c) to facilitate the isotropic release step.

The fabricated MEMS platform is found to allow precise control of the nanobeam displacement over 500 nm with ± 10 nm accuracy. The displacement of the MEMS actuator as a function of the applied voltage is measured using a custom-made image processing algorithm coupled with optical microscopy. Optical images of the MEMS are taken at a 50 \times magnification (see Figure 3a) for different actuation voltages.

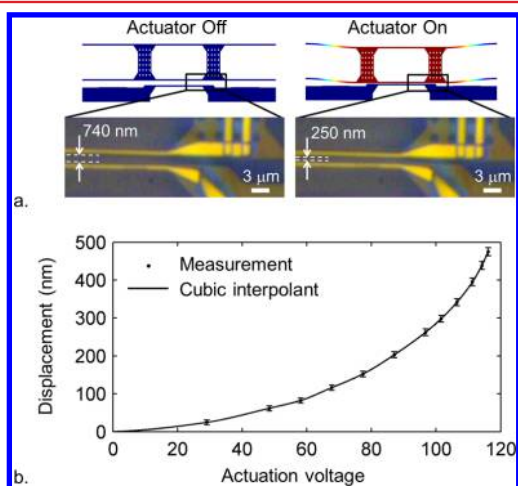


Figure 3. (a) Optical images of the MEMS displacement at actuation voltages of 0 (left) and 116 V (right). The images are treated by our image processing algorithm to extract the MEMS displacement. (b) Measured MEMS displacement as a function of the actuation voltage. The cubic spline interpolation is used to convert actuation voltages to displacement values.

The relative position of the two beams is then extracted by fitting Gaussian distributions over the nanobeam images. This fitting algorithm is repeated and averaged over all cross-section slices of each image file (i.e., over each vertical slice of the nanobeams in Figure 3a). The measured displacement of the mobile nanobeam is presented in Figure 3b, which shows smooth and continuous control of the MEMS position as a function of the applied voltage. The uncertainty on the measured displacement arises from the precision of the image processing algorithm (± 5.5 nm) and from the uncertainty on the scale of the image (67.8 ± 0.7 nm/pixel). The detailed calculation of these uncertainty values is presented in Supporting Information S1. It should be noted that, although we can measure the relative displacement of the MEMS with great accuracy, our knowledge of the absolute distance between the two nanobeams suffers from greater uncertainty due to our difficulty in evaluating the initial beam separation distance ($d_0 = 740$ nm). Although d_0 is fixed by design, it changes significantly upon release due to internal material stress and must therefore be evaluated from scanning electron micrographs of the released device. We also note that the maximum achieved displacement in Figure 3b is slightly below 500 nm, while the initial gap is around 740 nm, which means that the minimum achievable gap is in the 200–250 nm range. The reason why the gap cannot be reduced further is not fundamental and is detailed in Supporting Information S2.

Measurements of temperature changes as a function of nanobeam separation clearly indicate that near-field heat

transfer is the dominant thermal transport mechanism between the nanobeams. All heat transfer experiments are carried in vacuum at a pressure of 1.5×10^{-4} Torr. The electrical measurements are performed using an Agilent B1500A semiconductor device parameter analyzer. In the heat transfer experiment, the gap between the nanobeams is progressively reduced using the MEMS actuator, while a constant voltage of $V_{\text{fix}} = 0.22$ V is supplied to heat up the fixed nanobeam (which translates to $33 \mu\text{W}$ of electrical power at the initial beam separation). Meanwhile, the temperature of the mobile sensing beam is measured using a $10 \mu\text{A}$ sensing current (which translates to $0.12 \mu\text{W}$ electrical power, more than 2 orders of magnitude lower than the heating power applied to the fixed beam). To ensure that the system is in its steady state at each measurement point, a 0.2 s delay is included between the MEMS actuation voltage setting and the temperature readout. This delay is orders of magnitude larger than the thermal time constants of the fixed heated beam (1.3 ms) and the mobile sensing beam (7.4 ms). Those time constants were measured in a separated experiment by applying a step voltage variation to the nanobeam resistors while measuring their transient current. The temperatures of both nanobeams are calculated from the measured electrical resistance (R) of their platinum resistors, which changes as $\Delta R/R = TCR \times \Delta T$, where the temperature coefficient of resistance (TCR) is 0.00181 K^{-1} . The TCR value was calibrated separately by measuring the resistance of a device placed on a hot plate ramped from 20 to 150 $^{\circ}\text{C}$. The temperature (relative to room temperature) of both the fixed heated beam and the mobile sensing beam, as a function of their separation distance, is presented in Figure 4. As the gap

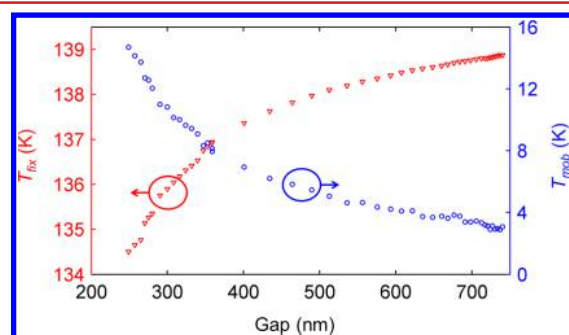


Figure 4. Measured temperature (relative to room temperature) of the fixed heated beam (T_{fix}) and the mobile sensing beam (T_{mob}) as a function of their separation distance. In this case, a constant heating voltage is supplied to the fixed beam, while only a sensing current is supplied to the mobile beam.

decreases, the temperature of the fixed heated beam diminishes slightly as it loses heat to the mobile beam. More importantly, the temperature of the mobile sensing beam increases by almost a factor of 5 (from $T_{\text{mob}} = 3$ K to $T_{\text{mob}} = 14.7$ K). Such increase is a clear indication that as the gap decreases, near-field effects, rather than conduction through the substrate, dominate heat transfer between the nanobeams (substrate conduction should indeed be gap independent).

The near-field heat transfer power is extracted from our temperature measurements and is found to be 8 times stronger than substrate conduction and 7 times stronger than the far-field radiation limit. We can convert the temperature data of Figure 4 to heat transfer power values (q) using eq 1, which is obtained by solving the equivalent thermal circuit of the

experiment (as is routinely done for on-chip thermal transport experiments³²).

$$q = \frac{P_{\text{fix}} X T_{\text{mob}}}{(T_{\text{fix}} - T_{\text{mob}})(T_{\text{fix}} + X T_{\text{mob}})} \quad (1)$$

In eq 1, q is the power transfer (in Watt/K) normalized by the temperature difference between the beams, T_{fix} and T_{mob} are, respectively, the temperature of the fixed heated beam and the mobile sensing beam, and $X = \sigma_{\text{mob}}/\sigma_{\text{fix}}$ is the ratio of the background heat conductions of the nanobeams. For each nanobeam, the background heat conduction between the beam and the substrate (i.e., σ_{mob} and σ_{fix}) is determined by applying a ramping electrical power to the beam while simultaneously measuring its temperature (i.e., its electrical resistance). The inverse of the slope of this temperature vs electrical power measurement yields the background conduction, in units of Watt/K. We obtain conduction values of $\sigma_{\text{fix}} = 237$ nW/K and $\sigma_{\text{mob}} = 107$ nW/K for the fixed heated beam and the mobile sensing beam, respectively. Using these values and the temperature data of Figure 4, we obtain the heat transfer power as a function of the nanobeam separation (see Figure 5).

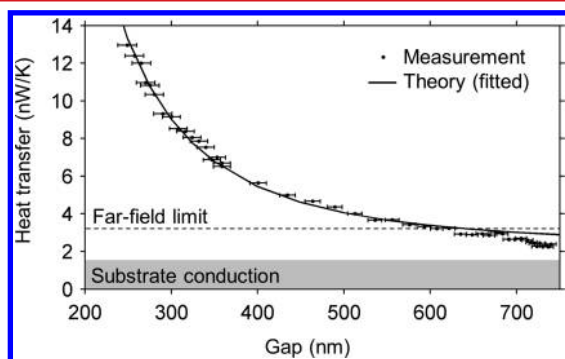


Figure 5. Heat transfer power between the nanobeams as a function of their separation distance. Substrate conduction is found to account for less than 15% of the total heat transfer at the smallest gap. Near-field heat transfer is also found to be 7 times stronger than the far-field limit (1.7 nW/K above the substrate conduction, for the current geometry and temperatures).

In Figure 5, the horizontal error bars correspond to the error on the measurement of the MEMS displacement (see Figure 3). Vertical error bars are not visible, as they are determined by the very high resolution of the Agilent device parameter analyzer. The theory curve is the same as in Figure 1, but is now translated horizontally and vertically to best fit the experimental data. The horizontal translation is included to account from our uncertainty on the initial distance (d_0) between the beams (see discussion related to Figure 3 and the MEMS displacement measurement), while the vertical translation accounts for spurious conduction of heat through the substrate. The translation that best fits the experimental data is +49 nm horizontally and +1.49 nW/K vertically. After fitting, the theory is found to correspond closely with the experimental data. Slight discrepancies between theory and measurements most likely arise from deviation of the beam cross-section from the perfectly rectangular shape considered in the simulations (see Figure 2d). The 1.49 nW/K substrate conduction obtained from the fit is included in Figure 5, from which we note that spurious substrate conduction account for less than 12% of the total heat transfer at the smallest gap. The far-field radiation limit (1.7 nW/K) is also included in Figure 5 in order to

illustrate the strong enhancement of heat transfer in the near-field compared to the far-field value. The far-field emission is obtained by the same Fourier modal method used in Figure 1.

We have presented the first demonstration of near-field radiative heat transfer between two integrated nanostructures and shown that near-field radiation can be the dominant heat transport channel between these structures, even on a fully integrated platform. The approach, based on nanobeam integration with MEMS actuation, could enable the development of new near-field thermal control devices, such as thermal rectifiers and thermal transistors.

■ ASSOCIATED CONTENT

📄 Supporting Information

- (1) Uncertainty on the MEMS displacement measurement.
 - (2) Discussion on the minimum achievable nanobeam separation.
 - (3) Supplemental calibration of the temperature measurement.
- This material is available free of charge via the Internet at <http://pubs.acs.org>.

■ AUTHOR INFORMATION

Corresponding Author

*E-mail: michal.lipson@cornell.edu.

Notes

The authors declare no competing financial interest.

■ ACKNOWLEDGMENTS

The authors gratefully acknowledge Clayton Otey for using some of his codes for the calibrations of the numerical simulations presented here. The authors gratefully acknowledge support from DARPA for award FA8650-14-1-7406 supervised by Dr. Avram Bar-Cohen. This work made use of the Cornell Center for Materials Research Shared Facilities, which are supported through the NSF MRSEC program (DMR-1120296), and of the Cornell NanoScale Facility, a member of the National Nanotechnology Infrastructure Network, which is supported by the National Science Foundation (Grant ECCS-0335765). R.S.-G. holds a postdoctoral fellowship from the Fonds de recherche du Québec—Nature et Technologies.

■ REFERENCES

- (1) Polder, D.; Van Hove, M. *Phys. Rev. B* **1971**, *4* (10), 3303–3314.
- (2) Loomis, J. J.; Maris, H. J. *Phys. Rev. B* **1994**, *50* (24), 18517–18524.
- (3) Pendry, J. B. *J. Phys.: Condens. Matter* **1999**, *11* (35), 6621.
- (4) Fu, C. J.; Zhang, Z. M. *Int. J. Heat Mass Transfer* **2006**, *49* (9–10), 1703–1718.
- (5) Volokitin, A. I.; Persson, B. N. *J. Rev. Mod. Phys.* **2007**, *79* (4), 1291–1329.
- (6) Francoeur, M.; Mengüç, M. P.; Vaillon, R. *Appl. Phys. Lett.* **2008**, *93* (4), 043109.
- (7) Rousseau, E.; Siria, A.; Jourdan, G.; Volz, S.; Comin, F.; Chevrier, J.; Greffet, J.-J. *Nat. Photon.* **2009**, *3* (9), 514–517.
- (8) Shen, S.; Narayanaswamy, A.; Chen, G. *Nano Lett.* **2009**, *9* (8), 2909–2913.
- (9) Rodriguez, A. W.; Ilic, O.; Bermel, P.; Celanovic, I.; Joannopoulos, J. D.; Soljačić, M.; Johnson, S. G. *Phys. Rev. Lett.* **2011**, *107* (11), 114302.
- (10) Kralik, T.; Hanzelka, P.; Zobac, M.; Musilova, V.; Fort, T.; Horak, M. *Phys. Rev. Lett.* **2012**, *109* (22), 224302.
- (11) Shi, J.; Li, P.; Liu, B.; Shen, S. *Appl. Phys. Lett.* **2013**, *102* (18), 183114.
- (12) Kittel, A.; Müller-Hirsch, W.; Parisi, J.; Biehs, S.-A.; Reddig, D.; Holthaus, M. *Phys. Rev. Lett.* **2005**, *95* (22), 224301.

- (13) De Wilde, Y.; Formanek, F.; Carminati, R.; Gralak, B.; Lemoine, P.-A.; Joulain, K.; Mulet, J.-P.; Chen, Y.; Greffet, J.-J. *Nature* **2006**, *444* (7120), 740–743.
- (14) Jones, A. C.; Raschke, M. B. *Nano Lett.* **2012**, *12* (3), 1475–1481.
- (15) DiMatteo, R. S.; Greiff, P.; Finberg, S. L.; Young-Waithe, K. A.; Choy, H. K. H.; Masaki, M. M.; Fonstad, C. G. *Appl. Phys. Lett.* **2001**, *79* (12), 1894–1896.
- (16) DiMatteo, R.; Greiff, P.; Seltzer, D.; Meulenberg, D.; Brown, E.; Carlen, E.; Kaiser, K.; Finberg, S.; Nguyen, H.; Azarkevich, J. In *Micron-gap Thermophotovoltaics (MTPV)*, Sixth Conference on Thermophotovoltaic Generation of Electricity: TPV6; AIP Publishing: Melville, NY, 2004; pp 42–51.
- (17) Laroche, M.; Carminati, R.; Greffet, J.-J. *J. Appl. Phys.* **2006**, *100* (6), 063704.
- (18) Basu, S.; Zhang, Z. M.; Fu, C. J. *Int. J. Energy Res.* **2009**, *33* (13), 1203–1232.
- (19) Ottens, R. S.; Quetschke, V.; Wise, S.; Alemi, A. A.; Lundock, R.; Mueller, G.; Reitze, D. H.; Tanner, D. B.; Whiting, B. F. *Phys. Rev. Lett.* **2011**, *107* (1), 014301.
- (20) Guha, B.; Otey, C.; Poitras, C. B.; Fan, S.; Lipson, M. *Nano Lett.* **2012**, *12* (9), 4546–4550.
- (21) Otey, C. R.; Lau, W. T.; Fan, S. *Phys. Rev. Lett.* **2010**, *104* (15), 154301.
- (22) Basu, S.; Francoeur, M. *Appl. Phys. Lett.* **2011**, *98* (11), 113106.
- (23) Iizuka, H.; Fan, S. *J. Appl. Phys.* **2012**, *112* (2), 024304.
- (24) Zhu, L.; Otey, C. R.; Fan, S. *Appl. Phys. Lett.* **2012**, *100* (4), 044104.
- (25) Wang, L. P.; Zhang, Z. M. *Nanoscale Microscale Thermophys. Eng.* **2013**, *17* (4), 337–348.
- (26) Park, K.; Zhang, Z. *Front. Heat Mass Transfer* **2013**, *4* (1), 013001.
- (27) Zhu, L.; Otey, C. R.; Fan, S. *Phys. Rev. B* **2013**, *88* (18), 184301.
- (28) Ben-Abdallah, P.; Biehs, S.-A. *Phys. Rev. Lett.* **2014**, *112* (4), 044301.
- (29) Poot, M.; Tang, H. X. *Appl. Phys. Lett.* **2014**, *104* (6), 061101.
- (30) Lussange, J.; Guérout, R.; Rosa, F. S. S.; Greffet, J. J.; Lambrecht, A.; Reynaud, S. *Phys. Rev. B* **2012**, *86* (8), 085432.
- (31) Otey, C. R.; Zhu, L.; Sandhu, S.; Fan, S. *J. Quant. Spectrosc. Radiat. Transfer* **2014**, *132* (0), 3–11.
- (32) Chang, C. W.; Okawa, D.; Majumdar, A.; Zettl, A. *Science* **2006**, *314* (5802), 1121–1124.